Available online at www.sciencedirect.com
ScienceDirect
Icarus 192 (2007) 378–395
ICARUS
www.elsevier.com/locate/icarus

High-resolution atmospheric observations by the Mars Odyssey Thermal Emission Imaging System

Ai Inada [a,*], Mark I. Richardson [a], Timothy H. McConnochie [b], Melissa J. Strausberg [c], Huiqun Wang [d], James F. Bell III [e]

[a] *California Institute of Technology, M.S. 150-21, 1200 E. California Blvd., Pasadena, CA 91125, USA*
[b] *NASA Goddard Space Flight Center, Greenbelt, MD 20771, USA*
[c] *University of California, Los Angeles, 7229 Math Science Bld., Los Angeles, CA 90095-1565, USA*
[d] *Harvard-Smithsonian Center for Astrophysics, MS-50, 60 Garden Street, Cambridge, MA 02138, USA*
[e] *Cornell University, Space Sciences Building, Cornell University, Ithaca, NY 14853, USA*

Received 28 February 2007; revised 29 June 2007

Available online 11 September 2007

Abstract

High-resolution observations of atmospheric phenomena by the Mars Odyssey Thermal Emission Imaging System (THEMIS) during its first mapping year are presented. An atmospheric campaign was implemented on the basis of previous spacecraft imaging. This campaign, however, proved of limited success. This appears to be due to the late local time of the Odyssey orbit (the locations of activity at 4–6 p.m. appear to be different from those at 2 p.m.). Ironically, images targeting the surface were more useful for study of the atmosphere than those images specifically targeting atmospheric features. While many previously recognized features were found, novel THEMIS observations included persistent clouds in the southern polar layered deposits, dust or condensate plumes on the northern polar layered deposits, dust plumes as constituent parts of local dust storms, and mesospheric clouds. The former two features tend to be aligned parallel and normal to polar troughs, respectively, suggesting a wind system directed normal to troughs and radially outward from the center of the polar deposits. This is consistent with katabatic drainage of air off the polar deposits, analogous to flow off Antarctica. The observation of dust lifting plumes at unprecedented resolution associated with local dust storms not only demonstrates the importance of mean wind stresses (as opposed to dust devils) in initiation of dust storms, but is also seen to be morphologically identical to dust lifting in terrestrial dust storms. As Odyssey moves to earlier local times, we suggest that the atmospheric campaign from the first mapping year be repeated.

Keywords: Mars, atmosphere; Mars, polar caps

1. Introduction

The Mars Odyssey Thermal Emission Imaging System (THEMIS) consists of multi-channel visible and thermal infrared cameras (Christensen et al., 2003, 2004). With a surface-projected pixel size of between 20 and 100 m, the THEMIS visible camera (VIS) fills an important spatial scale gap between the atmospheric images obtained with the Mars Global Surveyor (MGS) Mars Orbiter Camera (MOC) narrow angle (NA) camera at 1–10 m scale, and MOC wide angle (WA) cameras at 0.2–7 km scale (Malin and Edgett, 2001). The THEMIS infrared (IR) camera provides completely unprecedented thermal imaging at a projected pixel size of roughly 100 m. In principal, the THEMIS IR system allows the temperature contrasts within small-scale dynamical systems to be observed, as well as the derivation of dust and ice opacities at high spatial resolution. The purpose of this paper is to describe the atmospheric science campaign conducted by the THEMIS team during the first martian year of operations, and to describe some of the serendipitous atmospheric observations made in the course of geological observations. Indeed, this study presents the initial results of an examination of all visible images returned by THEMIS in the first mapping year (it proved more difficult to

* Corresponding author. Fax: +1 626 585 1917.
E-mail address: inada@gps.caltech.edu (A. Inada).

0019-1035/$ – see front matter
doi:10.1016/j.icarus.2007.07.020

detect atmospheric features in the IR than in the visible). In this light, this paper has been designed to be more of a "table of contents" regarding some of the more interesting or unique types of atmospheric phenomena evident in the THEMIS data set (to aid and assist in future work) than a detailed or exhaustive analysis of the data, though some assessment of mechanism is undertaken in certain cases.

While a great deal of information about the atmosphere can be gained from low-resolution, global observations such as those obtained from the MGS Thermal Emission Spectrometer (TES) and from the MOC WA daily global maps, a range of questions related to small-scale processes in the atmosphere can only be addressed with high resolution observations. Examples include: the detailed nature of water ice cloud formation, which can be constrained by examination of the cloud's high-resolution structure or "morphology" (e.g., do they resemble terrestrial cirrus clouds or diffuse hazes?); and the nature of dust lifting, which can be examined by observing lifting sites at high resolution.

THEMIS was launched to Mars in 2001 aboard the Mars Odyssey orbiter (Saunders et al., 2004). Odyssey began its primary mapping mission in March 2002, from a polar orbit with a roughly Sun-synchronous local time of 4–5 a.m./p.m. As a result, almost all THEMIS VIS data were collected in the late afternoon. The THEMIS VIS camera is a push-frame system with channels at 0.425, 0.540, 0.654, 0.749, and 0.860 μm. The THEMIS IR camera, which uses a pushbroom design with time delay integration, has ten bands, two at 6.78 μm, and one each at 7.93, 8.56, 9.35, 10.21, 11.04, 11.79, 12.57, 14.88 μm. Use of the IR camera data for retrieval of quantitative information on aerosols has already been described by Smith et al. (2003). THEMIS is a targeted instrument, in contrast with the essentially continuous global mapping data generated by TES (Christensen et al., 2001) and the MOC WA camera for daily global maps (Malin and Edgett, 2001). As such, observing interesting features requires a mixture of planning (using previous observations and model guidance) and serendipity—the latter ultimately being more important for THEMIS atmospheric results, as will be discussed.

The THEMIS instrument is fully described by Christensen et al. (2004). As such, in this paper we proceed directly (Section 2) to discussion of the targeting of observations for atmospheric science during the first mapping year. This targeting was largely based on lower-resolution imaging of Mars from previous years resulting from the MOC WA daily global maps (Cantor et al., 2002, 2001; Wang and Ingersoll, 2002, 2003). The results of this targeted survey are described. We then proceed (Section 3) to discuss the analysis of complete THEMIS VIS data set through to orbit 12665 (roughly the first 1.5 martian years of the mission). The VIS data were used to search the data set for interesting atmospheric features since it was found much easier to identify such features in the VIS rather than the IR frames. The VIS data set search yielded several hundred frames including unambiguous atmospheric features. The different types of dust and ice clouds have been categorized on the basis of composition and the likely dynamical process underlying these systems. In some cases terrestrial analogs are shown. A summary of results is provided in Section 4.

2. Atmospheric campaign plan

The THEMIS atmospheric campaign was conducted during the first year of mapping operations. The effect of the targeted campaign is evident in the distribution of THEMIS observations, especially for the visible images (for example, see Fig. 1), and thus the reasoning behind this distribution is worth some discussion. The THEMIS atmospheric targeting relied largely upon analysis of atmospheric images obtained by the MOC WA camera. Indeed, the THEMIS campaign can largely be viewed as an attempt to zoom in on the systems observed by MOC,

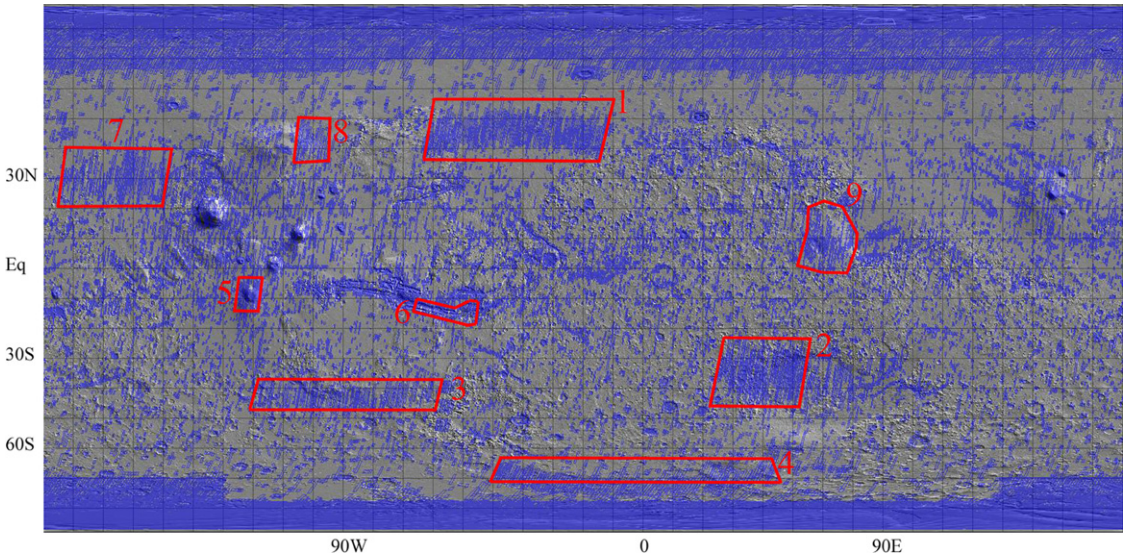

Fig. 1. A map of Mars showing the location of the atmospheric campaign Regions of Interest (ROI) and the distribution of THEMIS VIS frames collected during the first mapping year. The ROIs are numbered in accordance with their ordering in the text. Red boxes illustrate the ROIs, while the image outlines are indicated by blue boxes. The base map of shaded topography is provided for reference.

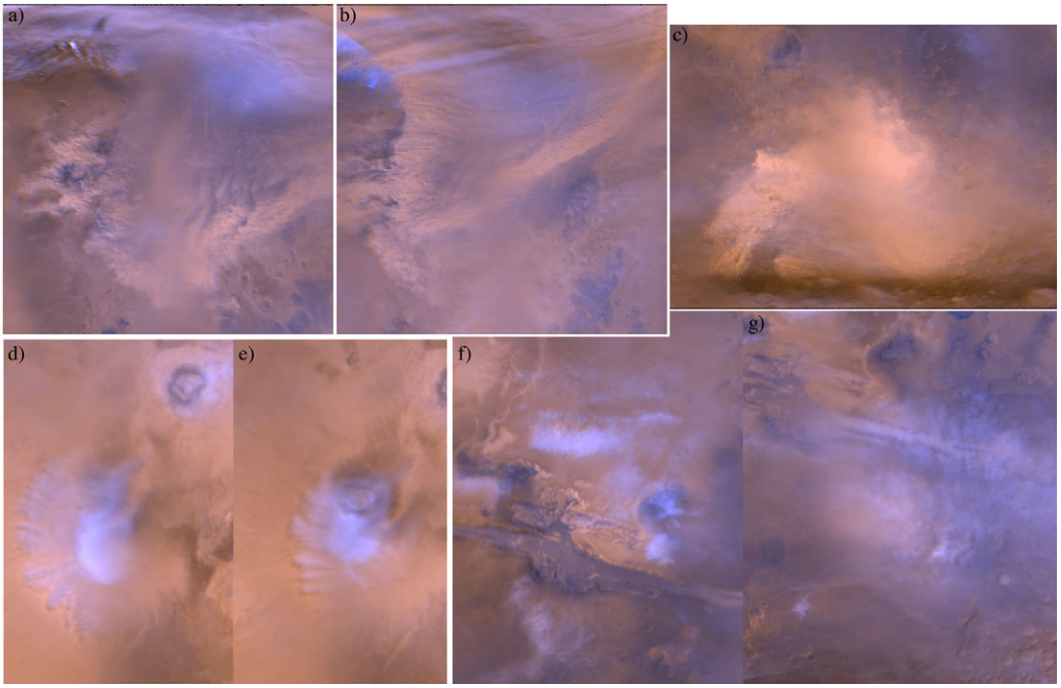

Fig. 2. A collection of MOC WA images that motivated part of the THEMIS atmospheric campaign. (a, b) Frontal dust storms observed in the northern hemisphere during late northern autumn and from mid to late northern winter to early northern spring (Wang et al., 2005). (c) Dust storm development on the rim of the Hellas basin [this event was part of the build up to the 2001 global storm (Strausberg et al., 2005)]. (d, e) "Flower clouds" or radially aligned water ice clouds observed to form over Arsia Mons. (f, g) Fogs and convective water ice clouds in Valles Marineris and on the surrounding regions. The blue color is enhanced.

and to extend the one- and two-color MOC images to a wider range of colors and into the thermal infrared. While the local times of the Odyssey and MGS orbits differ by roughly 2–3 h, the MOC data were viewed as the best available guide. In addition, the digested and analyzed MOC data available for THEMIS targeting were invariably derived from observations one or more martian years prior to the THEMIS imaging. As such, an effort was made to select only atmospheric phenomena that repeated regularly each year and with high frequency during their typical season(s) of activity. For example, frontal dust belts in the northern mid- and high-latitudes have been seen regularly in two seasonal windows in early to mid northern autumn and from mid to late northern winter to early northern spring (Cantor et al., 2002; Wang and Ingersoll, 2003; Wang et al., 2005), and thus were considered good candidates.

The THEMIS atmospheric campaign targets (or Regions of Interest—ROI), as enumerated in Fig. 1, were as follows (see Fig. 2 for examples of the MOC images used to motivate the ROI's):

1. Frontal Storm Survey. MOC Daily Global Map (DGM) mosaics (Wang and Ingersoll, 2002) from $L_s = 200°$–$250°$ and 290°–360° show planetary-scale dust fronts in northern high latitudes. These dust belts carry dust into the tropics and are believed to have been important to the growth of the largest dust storm of 1999 (Wang and Ingersoll, 2003). Though these images are relatively low resolution, it is still apparent that the dust belts are stirred by convection. Determination of the scale of this convection was a major goal for this target. The ROI specifically targeted the Chryse region, as this "storm track" (Hollingsworth et al., 1996) region was observed to be the most active by MOC in the first MGS mapping year (1999–2001).
2. Hellas Dust Monitoring. The Hellas basin is one of the most active regions of dust lifting on Mars, and the original center of major dust injection for the 2001 global storm (Strausberg et al., 2005). The goal of this ROI was to undertake detailed study of the morphology of dust lifting activity and comparison of visible and thermal high-resolution imaging. Differential tests for the importance of convection and wind stress lifting (Kahn, 1995) were envisioned.
3. Noachis Terra Survey. Noachis was the region of origin of a dust storm observed by MGS in 1997. This ROI was designed to capture potential dust lifting events in this area.
4. South Cap Edge Storm Survey. MOC images of the south polar cap edge show significant local dust lifting events and these have been mapped for the first year of MOC data by Cantor et al. (2001). The local storms likely arise due to the sharp thermal contrast between the polar ice cap and the adjacent surface, but may be locally augmented by topography. Information on the detailed structure of the lifting clouds, and the number of independent lifting plumes would yield insight into the ability of winds to exceed the lifting threshold and the nature of the local wind systems yielding lifting. Such south polar cap edge dust lifting events are thought to have triggered the 2001 global dust storm. The southern cap edge is also a site of previously observed water ice clouds—potentially low fogs or convective clouds resulting from outbreak of cold air from over the polar cap.

5. Arsia Mons Flower Cloud Survey. Radial water cloud structures were observed over Arsia Mons in MOC-WA near $L_s = 150°–180°$. The radial nature of these features indicates small-scale convective cells with fluid converging at the volcano base and diverging at some height. This height cannot be determined from the MOC data available, so one goal of the THEMIS study was to determine the depth of these features and to verify their convective nature.
6. Valles Marineris Fog and Convective Cloud Survey. Between $L_s = 150°–180°$, MOC-WA images demonstrate convective water ice clouds and morning fog. This ROI was designed to search for fogs in the canyon system and convective clouds systems in the regions north and south of the canyon system.
7. Amazonis Planitia Survey. Amazonis is the region of most active dust devil activity observed by MGS MOC (Cantor et al., 2006; Fisher et al., 2005). The Amazonis survey was designed to examine whether large dust devils were occurring in this area in the late afternoon. Some initial results of this survey (which were negative) have already been reported by Fisher et al. (2005) and Cantor et al. (2006).
8. Alba Patera Flank Cloud Survey. Topographically-forced clouds were observed to develop on the flanks of Alba Patera in early northern autumn by MOC, with this ROI designed to examine these systems at higher resolution ($L_s = 170°–200°$).
9. Isidis Planitia Rim Cloud Survey. In late northern summer, water ice clouds were observed to form on the rim of the Isidis basin by MOC. This ROI was designed to take a closer look at these clouds during the period $L_s = 135°–145°$.

The targeting of THEMIS based on MOC imagery was from the outset a calculated gamble: the local times of the parent spacecraft were different (4–6 p.m. vs 2 p.m.) and it was expected that there would be some variation in the location of observable meteorological phenomena with local time [e.g., when and where clouds form as predicted by a GCM (Richardson et al., 2002)]. However, in the absence of observations from which to make targeting predictions for the THEMIS local time, the MOC data provided the best reconnaissance. As things turned out, however, and despite the intensive survey of the ROI's, very few atmospheric features were observed by THEMIS as a result of the atmospheric campaign. Notable exceptions include the mesospheric clouds where the collection of multiple colors proved critical to quantitative analysis (McConnochie et al., in preparation), some convective/cumulus and lee-wave clouds, and some fogs.

In general, however, the THEMIS atmospheric campaign provided a negative result: meteorological systems and the conditions required to make them visible in the regions observed by MOC are inactive at the local times observed by THEMIS. Thankfully, THEMIS collected a large number of images aside from those of the atmospheric campaign. Ironically, these images have been much richer in terms of atmospheric phenomena, and some highlights are described in this paper, broken into different categories. Unfortunately, these images tended to be collected at higher resolution (thus over a smaller area), generally in only one color, and often without an infrared counterpart.

One point should be made on the naming convention used for the categories of atmospheric features recorded in this study. Naming is done in a manner that geologists would term "genetic": the name carries a suggestion of the mechanism responsible for the clouds based on our interpretation of cloud/haze morphology. While these mechanisms are those that we speculate created the clouds (we could well be wrong), the alternate naming convention by morphology (e.g., "puffy," "clumpy," "linear," "wispy") seemed somehow less desirable.

3. THEMIS atmospheric observations

The atmospheric phenomena observed by THEMIS in the visible by definition required a tracer to allow visualization: this visible tracer being dust and water ice aerosols. Thus, the features observed tend to be associated with either dust or water ice, and we have grouped phenomena associated with the two types of aerosols together. Within each aerosol type, a variety of phenomena were observed. We have examined every 30,625 VIS image collected by THEMIS during the first mapping mission from orbit 822 (20th Feb 2002) to orbit 12,665 (22nd Dec 2004) and roughly 8% of the total images contain atmospheric phenomenon. It should be noted that the concentration on polar phenomena is a function of the range of atmospheric phenomena found in the data set (more atmospheric phenomena were observed over the poles), but that this is largely traceable to the imaging bias in favor of the poles, due to the frequency of overflight and general interest of the science team in imaging the poles. Within the total data, 17.6 and 18.5% are devoted to the north polar (65°–90° N) and the south polar (65°–90° S) regions, respectively.

3.1. Condensate clouds

3.1.1. Polar clouds and fronts

In the high northern latitudes (65°–75° N) during late northern spring ($L_s \sim 45°–85°$), we observed several very crisp cloud "fronts": well developed and clearly delineated edges to thick clouds. Several examples of these cloud edges are provided in Fig. 3. In the images, the clouds are reminiscent of stratus clouds or fog banks. The edges of the clouds do not appear to be limited or constrained by topography. Nor do the clouds appear to be forced by surface topography or by surface albedo contrasts, therefore the sharp cloud edges correspond to a freely-moving interface between two airmasses.

The images show a fair amount of detail in the clouds. The fronts are not flat, but scalloped or textured, suggesting the presence of some limited turbulence. As one moves into the cloud from the edge, the thickness of the cloud can vary, and in different examples, "clumpiness" and regular lineation indicative of gravity waves can be seen to develop. The former indicated some amount of turbulence, while the latter may be due to wave forcing at the putative air mass front indicated by the cloud edge, or due to various unobserved surface forcing elements.

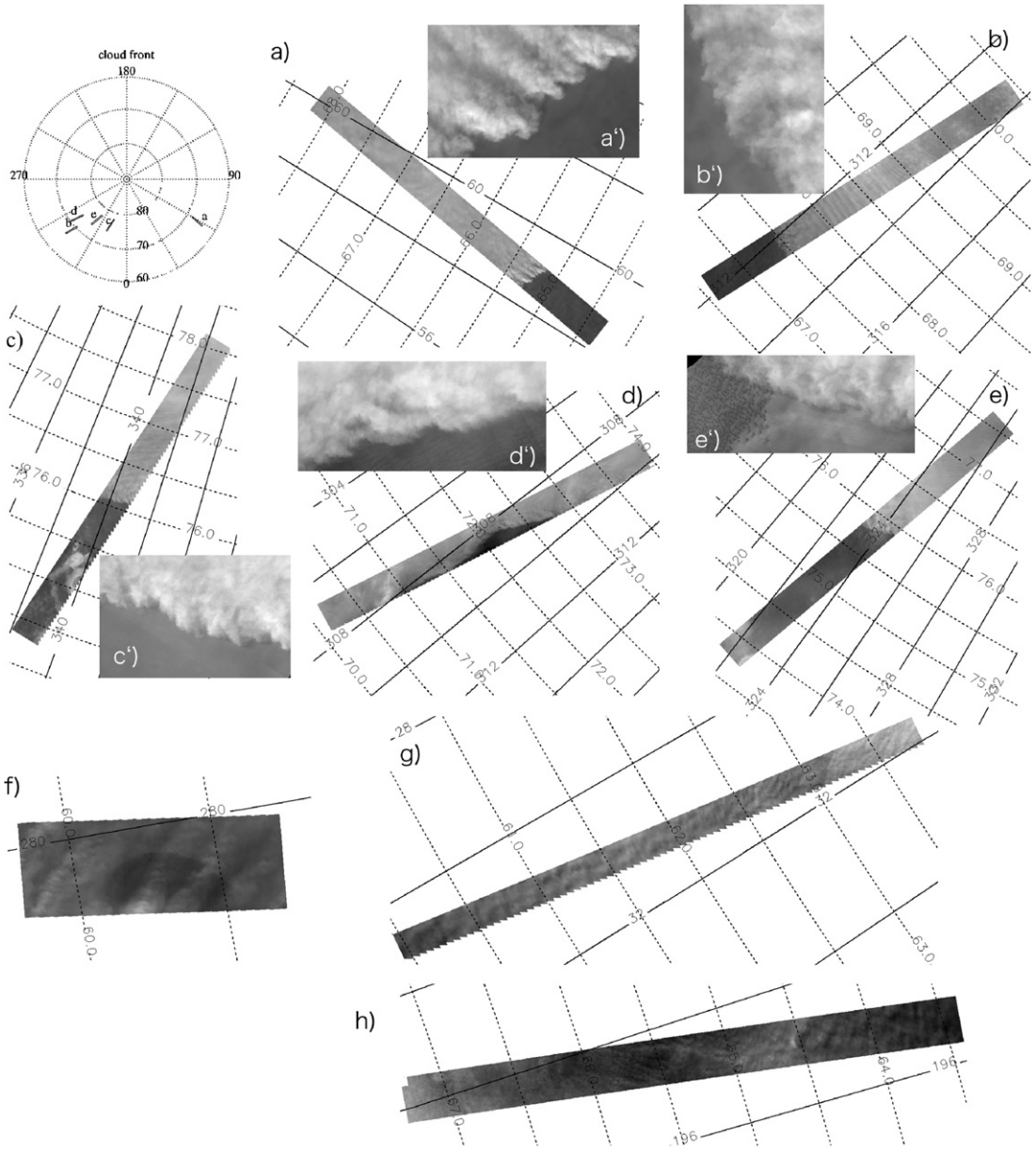

Fig. 3. THEMIS frames showing the edge and interior of the northern polar cloud in northern spring. Cloud edge images: (a) V11120003 ($L_s = 48°$), (b) V11261006 ($L_s = 53°$), (c) V12009037 ($L_s = 80°$), (d) V12010037 ($L_s = 80°$), (e) V12047006 ($L_s = 82°$). These positions are shown in the map at the top-left corner. Cloud insides images: (f) V10039008 ($L_s = 7°$), (g) V10447009 ($L_s = 23°$), and (h) V10616007 ($L_s = 30°$). Longitudes (solid lines) and latitudes (dotted lines) are marked every 2° and 0.5°, respectively.

Enhanced color MOC WA imagery provides not only an opportunity to assess the aerosol composition, but also to place the cloud fronts into context. Fig. 4 shows a portion of a MOC daily global map (DGM) image strip. The white appearance of the cloud system suggests a composition of water ice rather than dust (CO_2 can be ruled out on the basis of location and consequent thermal implications) and a mixture of dust and water ice at the edge. From MOC WA images, the clouds observed by THEMIS are seen to be quite extensive. Earlier in northern spring, these clouds appear associated with the hood over the cap. Later images show widespread low cloud extending just beyond the cap. Whether this latter cloud is still hood is likely a question of semantics—it seems plausible that these clouds form in the saturated airmass just above the exposed water ice cap in these latter frames. To the extent that the THEMIS frames are representative of the earlier polar hood, the presence of shadows very close to the clouds suggests that the cloud deck is located only a few hundred meters or so above the surface. Images from within the cloud deck show the kinds of structures seen near the edge, reminiscent of terrestrial stratus and stratocumulus clouds (Fig. 3).

We estimated the optical depth of the polar cloud by applying a 1-D radiative transfer model using the Spherical Harmonics Discrete Ordinate Method (SHDOM) (Evans, 1998). The surface in the southern part of Fig. 3a at around the latitude of 65° N is radiometrically flat and its Lambert albedo is estimated

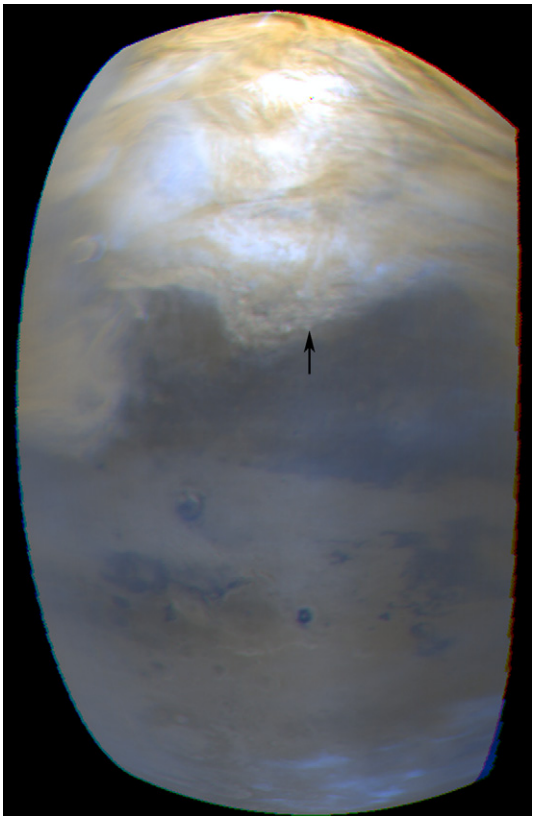

Fig. 4. Spherical projection of MOC WA images R1801409 and R1801410 (red and blue, respectively). The projection is centered on 60° N. The images are from the same day ($L_s = 48°$) and longitude as THEMIS image V11120003 (Fig. 3a). The arrow shows the point at 65° N, 59° E. The fronts shown in Fig. 3a correspond to the front of the polar hood, as shown in this figure. Although the cloud almost certainly contains dust (either independently or as cores of ice particles), the cloud has a strong signature in the blue channel, suggesting a water ice composition.

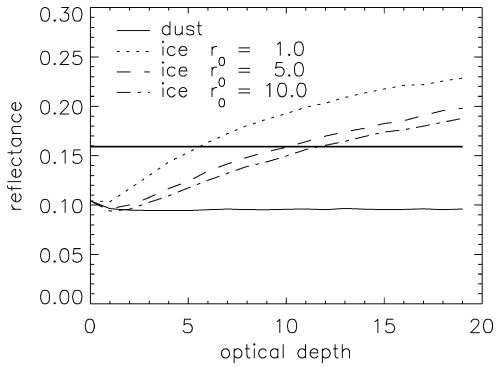

Fig. 5. Simulated reflectance of the bright atmospheric feature shown in Fig. 3a against optical depths with SHDOM. Solid line shows a case that it consists of dust particles, while dotted, dashed, and dot-dashed lines are for water ice particles with the mode radius of 1.0, 5.0, 10.0 μm, respectively. The reflectance of the observed cloud is given as the thick solid line.

to be 0.29 at a wavelength of 0.654 μm with the assumption of a clear overlying atmosphere. The reflectance (I/F) of the bright extended atmospheric feature (but not at the scalloped edge) is around 0.16. Reflectance (I/F) is defined as the ratio of the detected intensity to intensity reflected from a perfect Lambert surface illuminated at the zenith angle of zero degree. In this study, we analyze data only taken with band 3 (0.654 μm). The uncertainty in absolute radiance is less than 5% (2σ) based on a preflight calibration (McConnochie et al., 2006). The error is mainly caused by stray light, therefore the uncertainty in relative radiance is almost the same. While a detailed in-flight cross-check with data of the other instruments has not been established yet, THEMIS data were compared with those of Hubble Space Telescope (McConnochie et al., 2006). Although the result implies that the difference in viewing angles, spatial resolutions should be taken into account more carefully in future, we considered the uncertainty of the absolute photometric calibration in flight is less than 20%.

The first issue we wanted to examine was whether the cloud consisted of mainly dust or water ice particles (color from MOC WA already suggests the latter). Fig. 5 shows the calculated reflectance of a dust layer as a function of the dust optical depth. We used aerosol scattering properties derived from Imager for Mars Pathfinder data (Markiewicz et al., 1999). The angles of incidence, emission and phase are 68.92°, 0.35° and 68.85°. respectively. The maximum reflectance is 0.105 in the model (a Lambert albedo of 0.29 is used, as mentioned above), which is smaller than that of the observed cloud. As the dust layer thickens, the reflectance decreases slightly since the surface is quite bright. Throughout most of the range of optical depth shown, the reflectance for dust remains almost constant. As can be seen for the calculations of reflectance for water ice clouds of various sizes over the bright surface, the measured reflectance of 0.16 can be achieved for ice particle. Therefore, the clouds shown in Fig. 3 are primarily composed of water ice.

Secondly, the radiative model can be used to estimate the optical depth of water ice consistent with the observed reflectance. The retrieval is sensitive to the size distribution of ice particles, however the particle size in this image is unknown. We examine three cases, assuming the mode radii of water ice particles to be 1.0, 5.0 and 10.0 μm with a log-normal distribution. The scattering properties are calculated with the Mie theory using the refractive index from Warren (1984). The reflectance decreases as the ice particles grow (Fig. 5). The optical depths corresponding to the observed reflectivity are 5.6, 10.1, and 11.7 for the mode radii of 1.0, 5.0, and 10.0 μm, respectively. Even in a case that THEMIS overestimates the reflectance by 20%, the optical depths are still large as 3.5, 7.0, and 7.9 for the three cases. With the same manner, we estimated the optical depth of the other images give in Fig. 3. The results are shown in Table 1.

Fig. 6 shows the TES optical depths of dust and water ice over the region of Fig. 3a but observed two days before the THEMIS observation. Although the observation was performed at the different time, the TES profiles indicate that the front edge at 65.5° N consists of dust particles, and the main part has more water ice particles than the edge. Within the latitudes of 65°–67° N, the water ice opacity was about 0.13 ± 0.08, which is much smaller than the THEMIS VIS measurements. We attribute that the difference is mainly due to the wavelength difference as TES water ice opacity is measured at the wavelength of 12.12 μm. TES data acquired within five days after the THEMIS observations provides higher water ice opacity up

Table 1
Estimated optical depths of Northern polar clouds shown in Fig. 3

	File name	L_s	Lambert albedo	Optical depth		
				1.0 μm	5.0 μm	10.0 μm
a	V11120003	48	0.29 (0.23)	5.6 (3.5)	10.1 (7.0)	11.7 (7.9)
b	V11261006	53	0.25 (0.20)	5.2 (3.3)	9.1 (6.6)	10.7 (7.5)
c	V12009037	80	0.24 (0.19)	2.1 (1.5)	3.9 (3.2)	4.8 (3.7)
d	V12010037	80	0.19 (0.15)	3.0 (2.1)	5.3 (4.2)	6.3 (4.8)
e	V12047006	82	0.22 (0.18)	2.8 (1.9)	5.0 (4.0)	6.0 (4.5)

Particles are considered to be water ice with the mode radii of 1.0, 5.0, and 10.0 μm. Lambert Albedo is calculated from the image of the surface without clouds. The numbers in blankets are the Lambert albedo and the estimated optical depths in a case that THEMIS overestimates reflectance by 20%.

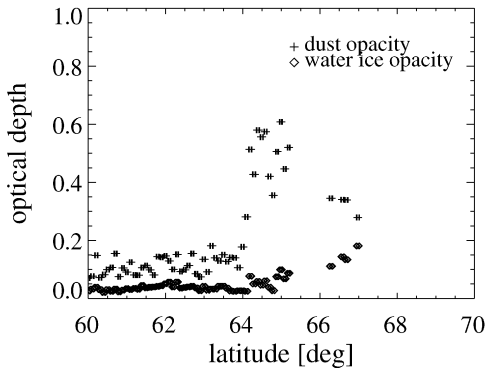

Fig. 6. Optical depths of dust and water ice in the region of Fig. 3a detected by TES two days before THEMIS observed there. The opacities for dust and water ice particles are at the wavenumbers of 1075 and 825 cm^{-1}, respectively. The dust optical depth increases at the latitude of 64° N and decreases to the north of 66° N, while the water ice amount gradually increases from 64° N toward the pole.

to 5.8 to the north of the latitudes 75° N, however the data flag indicates that the number is questionable due to surface ice.

It also should be noted that the optical depths of clouds with sharp edges is not typical for that of polar hood in this season. For example, 58 images in a latitudes of 64°–68° N were acquired within $L_s = 41°$–51°, and all of them display clouds or at least cloudy atmosphere. Among them, only 12 images show opaque clouds as Fig. 3a and no other images reveals the scalloped edge.

Table 1 shows that the polar clouds generally became thinner from the northern spring to the summer by factor two or more, although the absolute value depends on the assumed particle sizes.

3.1.2. Polar trough clouds

THEMIS acquired 1073 visible images of the south polar layer region at 75°–90° S, −120°–30° E during L_s = 240°–360° (southern summer) in the first observational year. Among them, 142 images revealed the presence of clouds that form in association with troughs. This type of clouds starts to form at $L_s = 251°$ and disappears after $L_s = 320°$. Almost all of the images with troughs observed during $L_s = 280°$–310° show clouds staying persistently along one side of them. Examples are provided in Fig. 7.

Initially, a challenge was in establishing whether these bright linear features overlaying a bright surface were in fact clouds, or whether they were surface features. The surface is covered by CO_2 ice with the Lambert albedo greater than 0.87. The images in Figs. 7a-1 and 7a-2 (V08674002 and V08699009) show the same location imaged two days apart (∼1.2° of L_s separated), with linear features present in both cases. However, the images show the exact location and detail of them to be different. Combined with the indication of shadows, this observation demonstrates that these are atmospheric features. Moreover the region of Fig. 7a (85.5°–86.5° S, 295°–308° E) has been observed 9 times from $L_s = 202°$ to $L_s = 312°$ in the first year of the observations, and 13 times between $L_s = 179°$ and $L_s = 336°$ in the second year. At $L_s = 202°$, the troughs were also covered by ice or it is too dark due to low solar altitude to recognize the contrast of the surface brightness clearly. After $L_s = 296°$, the troughs became darker than the surrounding area. Clouds appeared along them and stayed (Figs. 7a-1 and 7a-2) until $L_s = 312°$, when the last image of this area in the first year was taken. These clouds are even brighter than the surface with the reflectance of 0.39 at such a large incidence angle of 68.7°. Next year, the same kind of clouds appeared at $L_s = 303°$, but later images look very dusty and no clouds are identified. At $L_s = 334°$, the atmosphere becomes clearer, however a feature appeared between the two ends of troughs are dark and unlikely clouds. Other examples are also shown in Fig. 7.

The shadows suggest the clouds are low, at about 600 m from the surface. The occurrence of clouds associated with each trough in a given image, and their recurrence in repeated imaging demonstrates that these clouds are extremely persistent and must be associated with the typical state of the atmosphere for ∼30° of L_s after the seasonal polar frost and ice over troughs sublimates at $L_s \sim 270°$ (e.g., Litvak et al., 2007). To be more specific, the atmosphere must always be near saturation in this region such that a perturbation yields cloud formation, and the wind must consistently blow in a direction roughly perpendicular to the troughs. A schematic view of the cloud formation is given in Fig. 8. It is possible that humidity is locally derived from the exposed regolith (i.e., from water vapor released from the regolith), as analysis of THEMIS IR and OMEGA/Mars Express spectra imaging shows water ice present very near the surface in the southern pole (Bibring et al., 2004; Titus et al., 2003). Without high resolution atmospheric water vapor observations, it is not possible to decide, but observations with Compact Reconnaissance Imaging Spectrometer for Mars (CRISM) aboard Mars Reconnaissance Orbiter (MRO) may be able to address this.

The orientation of the clouds consistently on one side of the troughs suggests a persistent wind flow pattern normal to the troughs. While it seems clear that the troughs are forcing the clouds, what aspect of the trough is responsible and by what mechanism? The topographic depression that defines the troughs is an obvious answer, but there is also a substantial thermal contrast between the trough (exposed regolith) and the surrounding CO_2 ice, which is held at the condensation point temperature. This contrast could lead to substantial up-

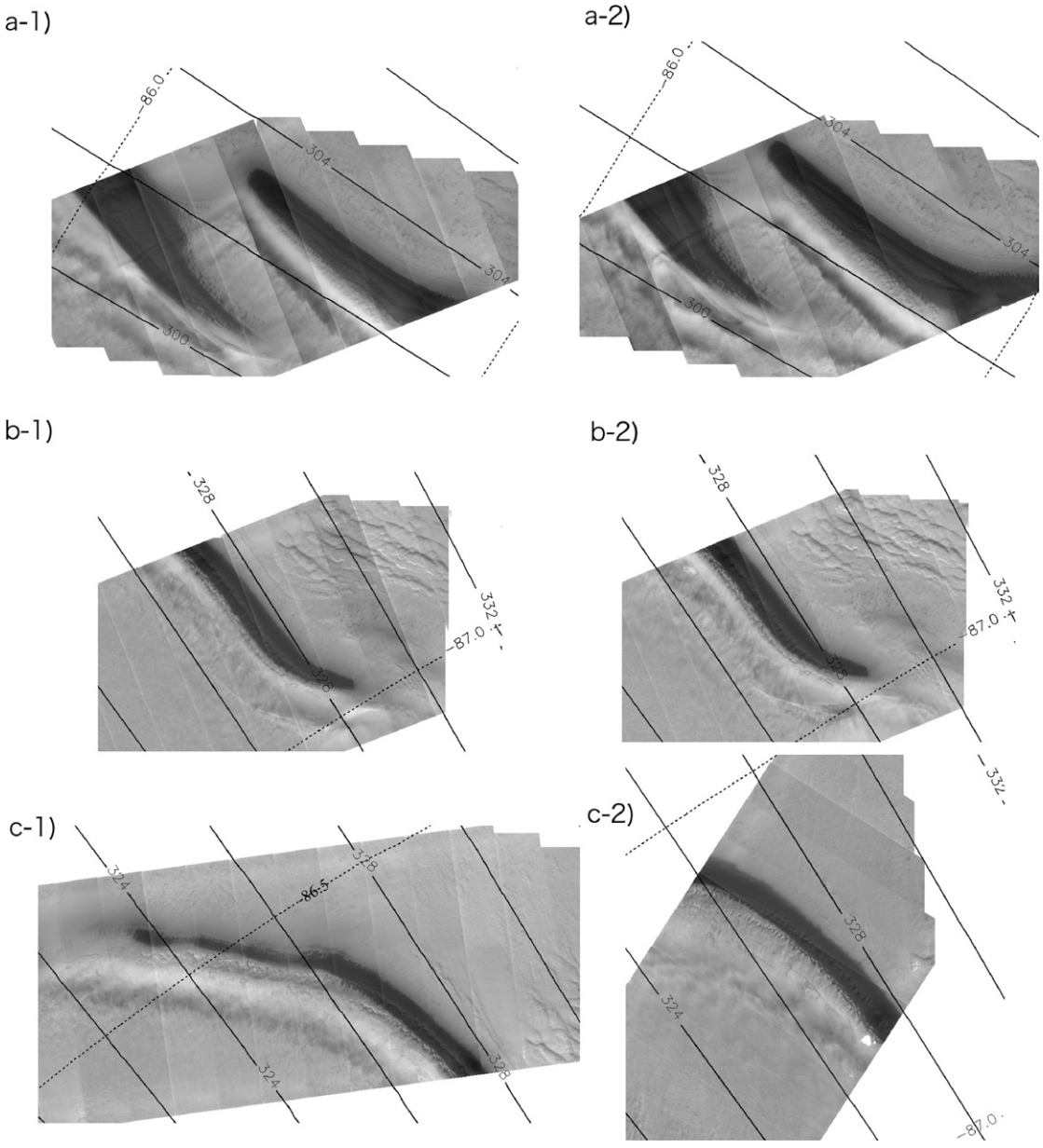

Fig. 7. THEMIS images showing trough-related clouds above the southern polar cap in southern summer. The left and right figures in each raw show the same region. (a-1 and b-1) V08674002 ($L_s = 307°$), (a-2 and b-2) V0869909 ($L_s = 308°$), (c-1) V08686007 ($L_s = 307°$), (c-2) V08825009 ($L_s = 314°$). Longitudes (solid lines) and latitudes (dotted lines) are marked every 2° and 0.5°, respectively.

slope flow of air heated at the bottom of the trough, and pushed to one side of the trough by the large-scale winds. Depending on the wind speeds across the trough and the nature of the flow in the trough, it may or may not be possible for air to pool there long enough for this mechanism to operate (i.e., for the trough-bottom air to heat sufficiently), while direct flow deformation due to topography would seem unavoidable. In either case, it can be seen in several of the images that more than one band of cloud can develop, suggesting the importance of gravity wave development for the cloud formation.

3.1.3. Lee wave clouds

To the extent that the "trough clouds" described in Section 3.1.2 are simply lee wave clouds, they constitute part of a wider category of clouds observed by THEMIS. Fig. 9 shows examples of lee wave clouds observed at various locations on the planet. Since lee wave clouds have been extensively documented in previous studies of Viking, Mariner 9, and MGS imagery (Briggs et al., 1979; French et al., 1981; Kahn, 1984; Pirraglia, 1976; Wang and Ingersoll, 2002), we will only note their presence in the THEMIS VIS archive.

3.1.4. Mesospheric clouds

In the introduction it is stated that the THEMIS VIS camera uses a push-frame approach, where the same portion of the surface is imaged in different color bands at slightly different times as the spacecraft moves along track. The slight resultant parallax between individual color frames has been used to

measure the heights of a limited set of clouds (McConnochie, et al., in preparation). By exploiting the time delay between individual frames, information on the zonal wind speeds is also derived. The clouds are sufficiently high (>45 km) that they are forming in the mesosphere of Mars (Zurek, 1992),

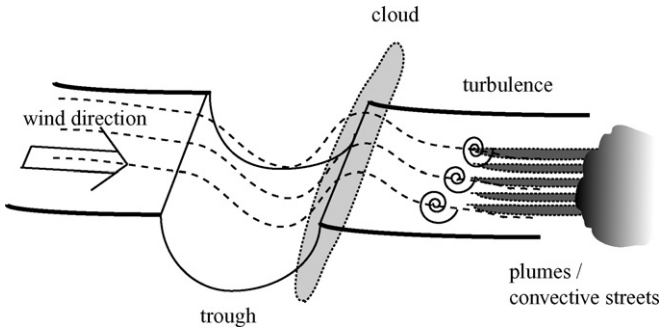

Fig. 8. Schematic view of a cloud formation along a trough and plumes aligned normal to a trough. When wind blows over trough normally, a perturbation due to the topography induces cloud formation in a saturated atmospheric layer. If the wind is strong enough to uplift dust particles from the surface or there are sufficient amount of water ice particles advected, plumes become visible parallel to the wind direction.

and are thus well above the height of most of the clouds examined in this paper (which are known through shadow measurements to be within a few km of the surface). Mesospheric clouds and hazes have been previously observed in a variety of forms and by instruments ranging from the Viking era to the present. These observations include; dust and detached condensate limb-hazes up to 90 km altitude observed in the visible by Viking (Jaquin et al., 1986; Jaquin, 1989); discrete clouds with shadows implying >50 km altitude observed in the visible by Viking (James, 1982) stellar occultation measurements by the SPICAM ultraviolet spectrometer on the Mars Express orbiter which show detached aerosol hazes in the 80–100 km altitude range (Montmessin et al., 2006); limb observations by the Mars Global Surveyor TES visible bolometer that show equatorial detached hazes in the 60–80 km altitude range (Clancy et al., 2007). However, given the present state of knowledge, these diverse observations may well reflect diverse phenomena, rather than multiple manifestations of the same phenomenon, and it is not clear that any of them correspond to the clouds observed by THEMIS VIS.

Two classes of mesospheric clouds have been observed. The first class (Fig. 10a) consists of equatorial clouds observed at a

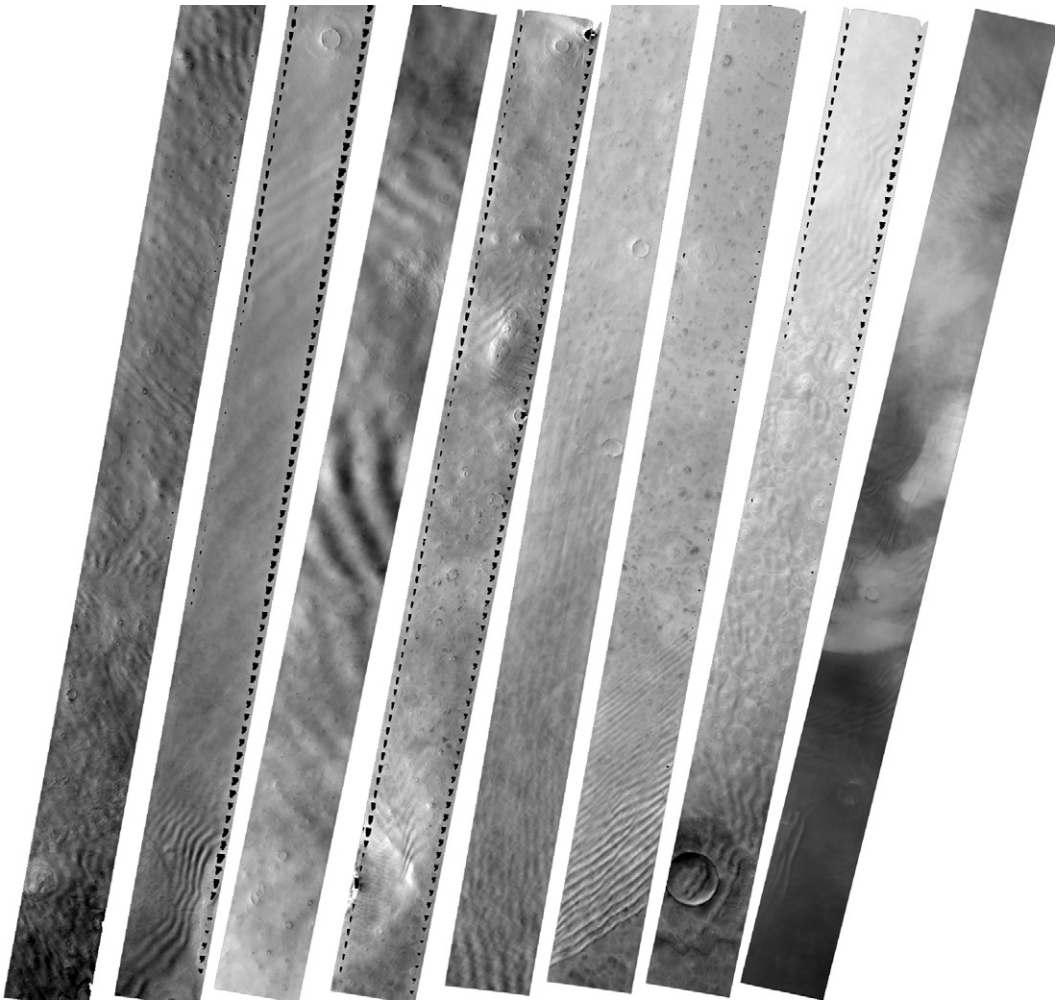

Fig. 9. Examples of gravity wave/lee wave clouds observed in the high northern latitudes in northern spring. From left to right are THEMIS frames: V10545003, V10582012, V10608013, V10681039, V10721002, V10743003, V11195005, and V11713001.

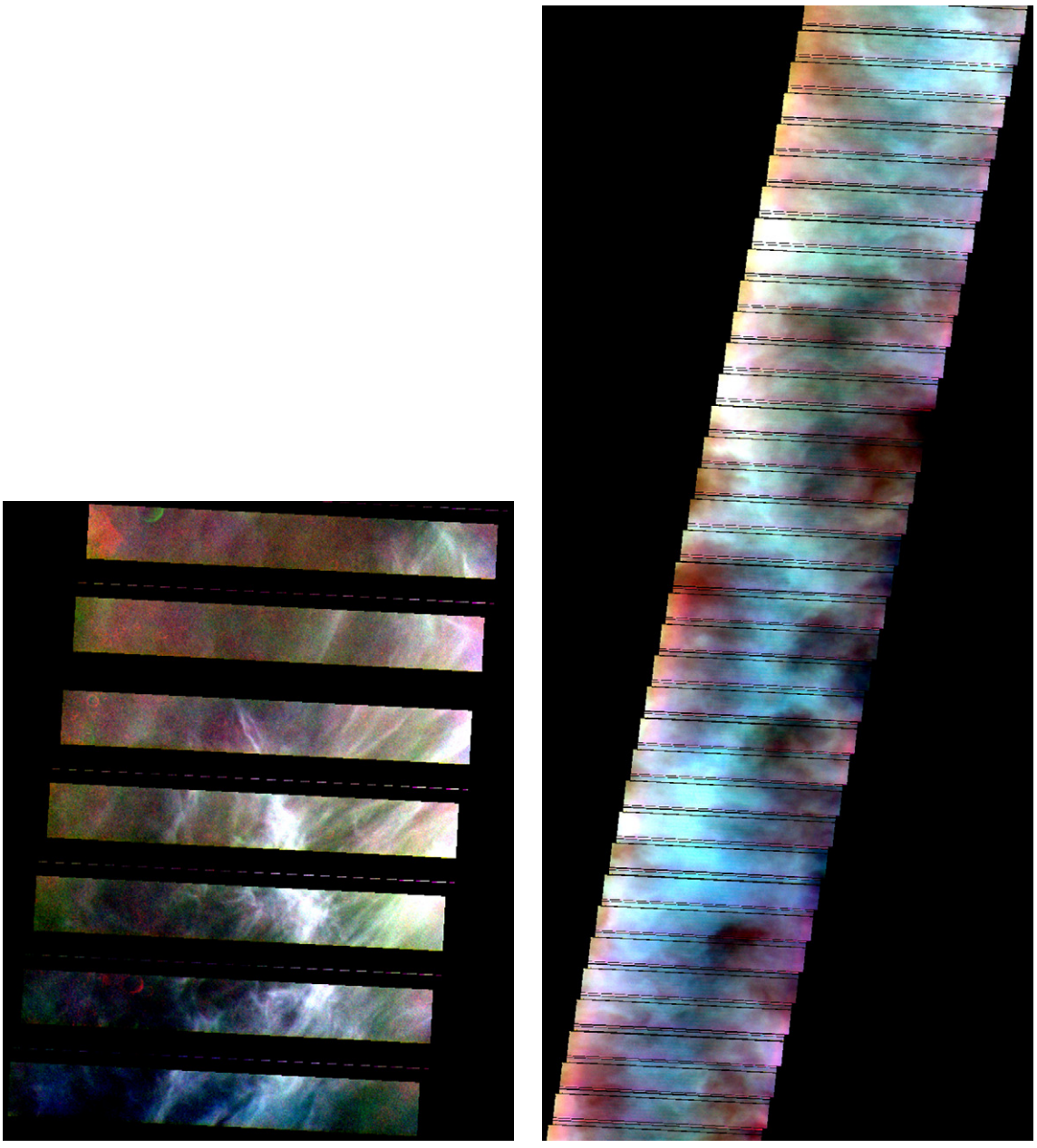

(a) (b)

Fig. 10. (a) Equatorial cloud features at an altitude of 80 km above the reference geoid with no measurable zonal velocity. Shown is a portion of THEMIS VIS image number V04573003 (16° S, 261° E, $L_s = 114°$) that has been map-projected onto the 80 km altitude surface. The individual frames that make of the image do not overlap at this altitude, causing gaps in the image. For scale, each frame is approximately 18 km wide in the east–west direction. The map-projection is simple cylindrical, with north at the top. Illumination is from the left (west) at an incidence angle of 80°. "Enhanced" color is used, meaning that each channel has been stretched individually to maximize contrast, with the 0.425, 0.540, and 0.654 μm bands controlling the blue, green, and red channels, respectively. (b) Northern mid-latitude winter cloud features at an altitude of 70 km above the reference geoid with an eastward zonal velocity of 60 m/s. Shown is a portion of THEMIS VIS image number V06930045 (47° N, 309° E, $L_s = 217°$) that has been map-projected onto the 70 km altitude surface. Individual exposures in the imaging sequence have been shifted to compensate for the 60 m/s zonal velocity. The individual frames that make of the image do not overlap at this altitude, causing narrow gaps in the image that appear as thin lines of missing data. For scale, each frame is approximately 18 km wide in the east–west direction. The map-projection is simple cylindrical, with north at the top. Illumination is from the left (west) with an incidence angle near 97° at surface elevation. Lower altitudes are in shadow. "Enhanced" color is used.

wide range of seasons. These clouds were observed serendipitously in surface-targeted multi-spectral VIS images, and are rare in the VIS data set, with only 5 examples identified out of a total of 2048 multi-band equatorial imaging sequences to date. Altitudes in the class range from 60 to 80 km above the reference geoid, and all examples show periodic lineated structures suggestive of wave activity. Propagation of gravity waves into the mesosphere is indicated in spacecraft entry data (Schofield et al., 1997), and may be of importance for the thermal structure and dynamics of the middle atmosphere—their detection in the THEMIS images is therefore interesting. The great height of these clouds leads to questions of their composition. Pathfinder

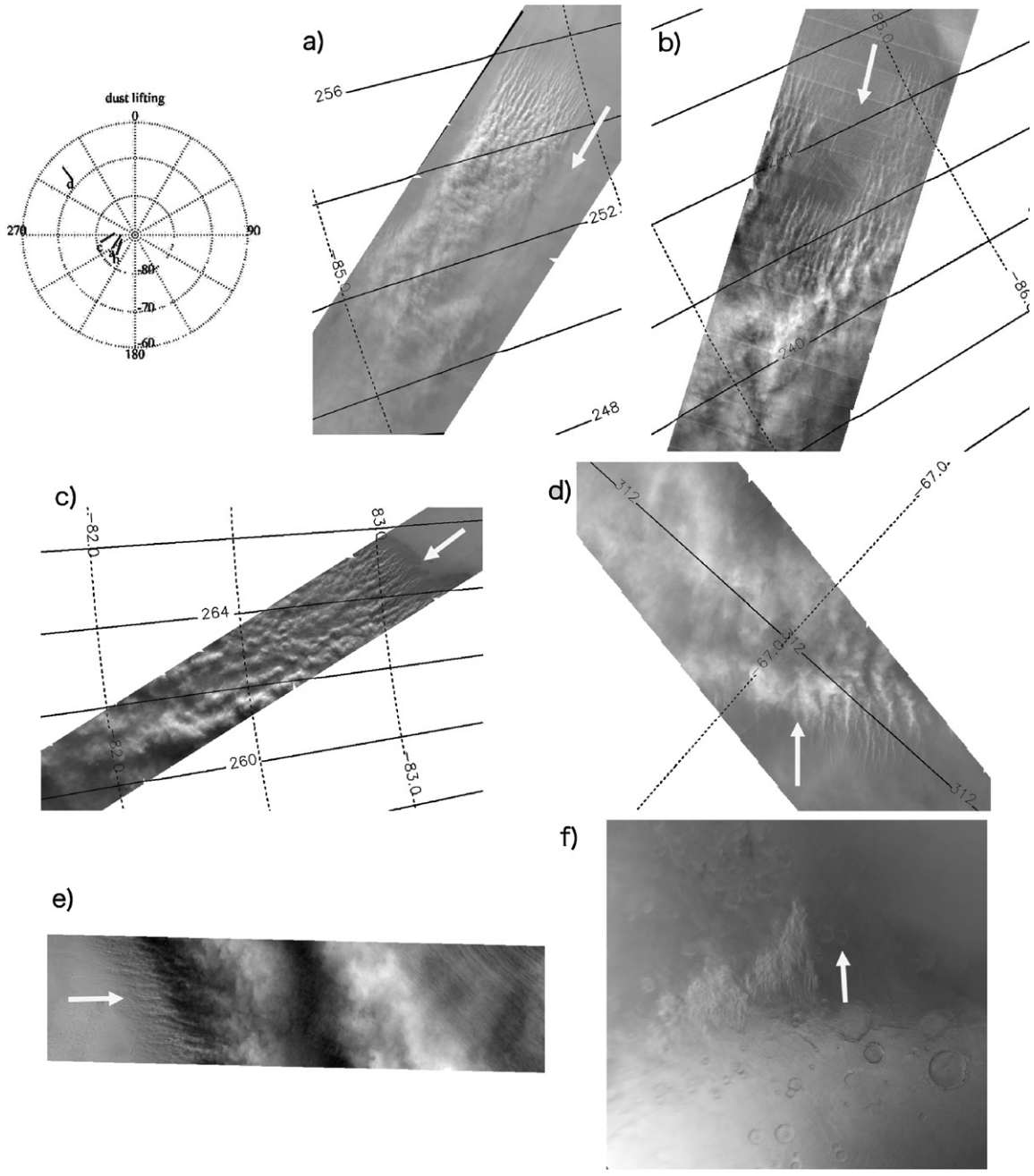

Fig. 11. Dust lifting within local dust storms as images by THEMIS and MOC in the southern high latitudes in southern summer. The arrows show the wind directions. THEMIS images: (a) V08463005 ($L_s = 296°$), (b) V08501007 ($L_s = 298°$), (c) V08874006 ($L_s = 316°$), and (d) V10113003 ($L_s = 10°$). (e) MOC NA E1101671 has four times the resolution of the THEMIS frames at the center of (185.1° E, 86.9° S) at $L_s = 288°$. (f) MOC WA E0501975 at the center of (53.2° E, 55.3° S) has previously been described by Strausberg et al. (2005). Although the image was observed at southern winter ($L_s = 182°$), it is believed to show the same kind of dynamics since the storm occurred near the seasonal polar cap. Longitudes (solid lines) and latitudes (dotted lines) are marked every 2° and 0.5°, respectively.

observed clouds in the tropical atmosphere at twilight when the surface was in darkness (Smith et al., 1997). Although Smith et al. (1997) interpreted these clouds as low-altitude indirectly illuminated water ice clouds, Clancy and Sandor (1998) suggest that these clouds were actually directly illuminated and at an altitude of roughly 80 km. Based on the altitude and entry profile temperature data, Clancy and Sandor (1998) go on to argue that these clouds are composed of CO_2 ice particles rather than water ice. It seems plausible that this first type of THEMIS mesospheric clouds provides a further example of the clouds imaged by Pathfinder.

The second class (Fig. 10b) are observed commonly in frontal storm campaign images, but only in twilight, with solar incidence angles greater than 90° at the elevation of the surface. These cloud features have altitudes up to 70 km and lack the linear periodic structures of the equatorial class. The kinds of clouds targeted by the frontal survey were associated with baroclinic storms (Wang et al., 2005), and while it is known

that baroclinic instabilities can be very deep on Mars (Barnes et al., 1993), the great height of the THEMIS clouds suggest they may be unrelated to the storm fronts observed by MOC and may be associated with vertically propagating waves (e.g., tides, Rossby waves).

3.2. Dust lifting

3.2.1. Dust plumes and storms

Several dramatic images of dust lifting were acquired over the southern pole in southern summer (Fig. 11). The capturing of these events near the CO_2 ice cap is likely a result of two factors. It is known that there is a distinct increase in the number of dust lifting and storm events near the edge of the seasonally-varying ice cap (Cantor et al., 2001)—taken to be a result of the thermal contrast across the cap edge and the consequently strong "sea breeze" circulations (Burk, 1976; Siili et al., 1997). There was also a distinct concentration of THEMIS imaging on the southern cap during summer, increasing the chances of catching lifting events that occurred there (Fig. 11d is sufficiently far from the cap that the cap thermal contrast is not likely of importance in this case).

The THEMIS dust plumes fit within a scale spectrum between those sampled by the MOC NA and WA cameras. In addition to the plumes observed by THEMIS, Fig. 11 shows a previously published WA image of a seasonal cap edge storm precursor to the 2001 global storm (Clancy et al., 2007; Strausberg et al., 2005) and a NA image of plumes. Based on Viking images, James (1985) proposed that lobate structure of dust storms at the cap edge was produced by a cold air current of undercutting warmer air by analogy with terrestrial haboobs. He also found that storms were moving away from the cap. More recently, Strausberg et al. (2005) used the suggestion of plume sources in the WA image to argue that the cloud suggests low-level flow off the cap, with downwind turbulent development and mixing of the plumes. While the relatively low resolution of the WA image prevented a firm conclusion, the resolution spectrum presented here (to the extent that they sample the same kind of phenomena) confirms this interpretation.

It is interesting to compare the martian plumes with plumes observed during dust storms on the Earth. Fig. 12 also shows a Moderate Resolution Imaging Spectroradiometer (MODIS) image of a dust storm that developed over northern Iraq in January 2006. The plume morphology is extremely similar to that of the plumes seen in the THEMIS imaging. Further, the low level winds for the Iraqi storm are known to be from the plume heads in the northwest towards the southeast. Rather unsurprisingly the plume heads are upwind of the more diffuse dust clouds, and thus it seems likely that this same directionality can be inferred for the martian dust plumes. The martian plumes are also rather similar in morphology to smoke plumes from terrestrial forest fires, which again have similar directional relationships.

The reason that dust lifting tends to form into plumes is that the turbulent mixing in the boundary layer tends to become organized into "streets" or rolls when a strong mean wind is active. This organization tends to imprint a pattern of surface stress perturbation minima and maxima, and also a strong horizontal convergence of lifted dust into the lines of surface-level upwelling. Some activity occurs at a range of spatial scales, but most activity tends to occur at the scale of the largest eddy (limited by the depth of the mixed layer). Fig. 13 shows a THEMIS image of dust plumes that has been used to measure the plume spacing. Typically, the aspect ratio of rolls over land (as measured on and modeled for the Earth) is about 1–4, i.e., the roll is one to four times wider than its depth (Young et al., 2002). The typical spacing of about 650–700 m (±100–200 m) implies a mixed layer depth of at most a little less than 1 km and possibly less than 200 m.

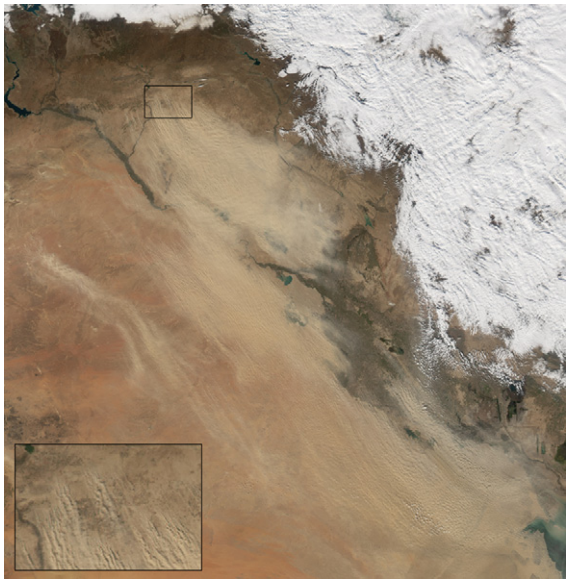

Fig. 12. An image of dust lifting over Iraq collected in January 2006 by the Aqua Moderate Resolution Imaging Spectroradiometer (MODIS) instrument. The plumes of dust lifting (see also insert) closely resemble those seen in the THEMIS images. The direction of mean wind is known to have been from northwest to southeast over Iraq during this storm.

3.2.2. Dust lifting from the northern polar layered deposits

During summer in the northern polar regions, plumes were observed that are generally aligned normal to trough features. Fig. 14 shows examples of plumes of aerosol emanating from the northern polar cap in early northern summer (the examples shown here are from within 6° of L_s of summer solstice). Figs. 14a and 14b were observed at the same day of $L_s = 91°$, and Figs. 14c and 14d were obtained with a 2-h difference at $L_s = 96°$. Fig. 14a revealed that wind from the North Pole make streets across the troughs in the north and south parts in this figure and finally cause a dust storm at the latitude of 81.5° N. From the fact that the plumes or linear structures appear to become lower the closer one gets to the head of the plume, a surface source for the aerosols (rather than condensation in the atmosphere) seems likely. This could still either be dust or loose particulate ice on the surface. The coincidence of the plume heads with dark troughs would seem to be further evidence for a dust composition. The transition, evident in some of the images, from a laminar flow of nearly straight, parallel plumes into widespread and somewhat deeper cloud must be an inherent feature of the flow in which the plumes are embedded.

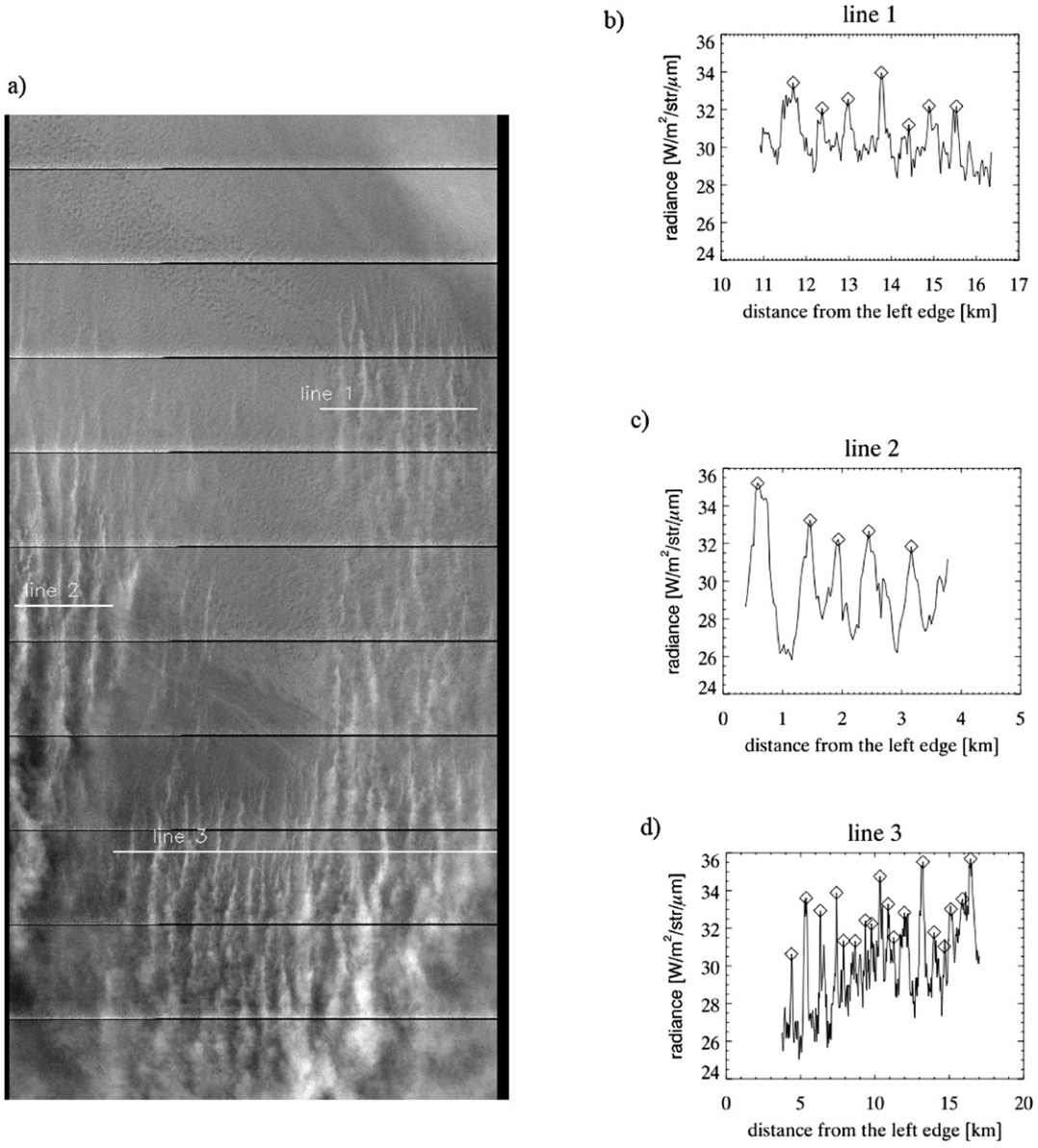

Fig. 13. Measurements of the spacing of the plumes in (a) THEMIS image V08501007. (b–d) Reflectance as function of distance along three plume clusters, illustrated by lines 1–3 (a). The average plume spacings were found to be: for line 1, 0.64 ± 0.10 km; for line 2, 0.65 ± 0.19 km; and, for line 3, 0.71 ± 0.25 km.

How the topography of the troughs and the thermal contrast due to the albedo difference between the troughs and the surrounding ice sheets play into this, is a worthy topic for future modeling (although it should be noted that laminar-to-turbulent transitions are a well-known feature of laboratory fluids and of dust storms and forest fire smoke on the Earth).

Figs. 14b, 14c, and 14d show clouds that developed over a trough at 87.0° N over a time span of a few days, just after northern summer solstice. In the first frame (Fig. 14b), a bright linear feature formed along the edge of the trough. We measured the optical depth of this cloud in the same manner described in Section 3.1.1. The Lambert albedo of the trough deposit is estimated as 0.41. The reflectance of the linear feature is 0.20, and hence it is too bright to assume the composition to be dust particles (as shown in Fig. 15a). It more likely consists of water ice and the estimated optical depths are 1.3–6.9, 3.6–12.7 and 4.2–15.0 with the assumed mode radii of 1.0, 5.0 and 10.0 μm, respectively. The lower limits are calculated in a case that THEMIS signals were overestimated by 20% of I/F. It should be noted that the cloud are illuminated from the surrounding icy surface where no clouds overcast, which is not taken into account in our scattering model. Hence the optical depth of an isolated cloud is more questionable than that of a spread cloud like a polar hood. A few days later, Fig. 14c reveals that the inside of the trough was clear, but that streets of atmospheric haze had developed perpendicular to the trough, with the streets merging and becoming diffuse beyond the trough (in a manner similar to that of Fig. 14a). The clumpy features to the south of the trough were over surface ice. The Lambert albedo of this surface was estimated to be 0.72, from the observed clear bright surface to the north of the trough. Both the morphology of the cloud and the optical depth modeling (Fig. 15b) suggest

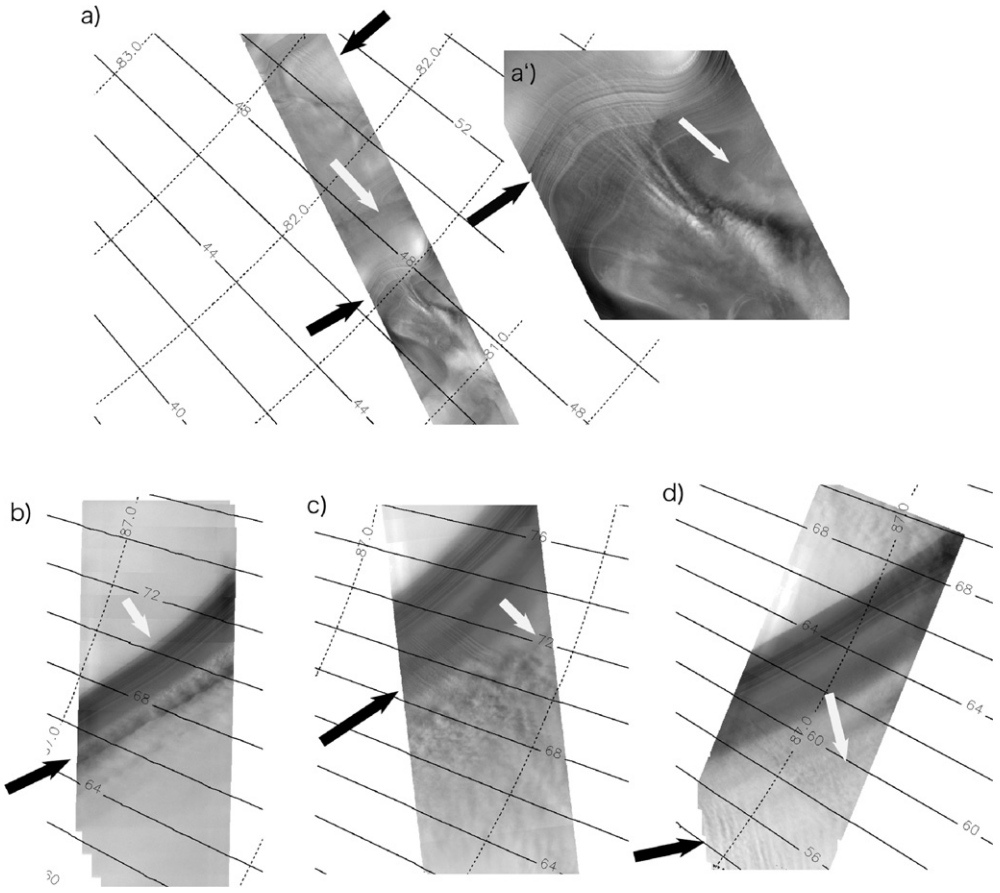

Fig. 14. Dust and/or particulate ice streaks and plumes over the northern polar cap in early northern summer. THEMIS frames: (a) V12294002 ($L_s = 91°$) with an enlarged dust storm, (b) V12295001 ($L_s = 91°$), (c) V12432001 ($L_s = 96°$), and (d) V12433003 ($L_s = 96°$). (b), (c) and (d) are at almost the same location and (c) and (d) were acquired within 2 h. Longitudes (solid lines) and latitudes (dotted lines) are marked every 2° and 0.5°, respectively. White allows show the wind directions, while black allows indicate interesting features.

that it likely consists of dust particles with an optical depth of 0.81 ± 0.09. The error estimated from the uncertainty in photometric accuracy of band 3 is much smaller than that for the water ice cloud because of a sharp negative function of the reflectance against optical depth between 0 and 3 over such bright ice as shown in Fig. 15. After 2 h, this dynamic activity settled down (Fig. 14c) and the optical depth to the south of the trough became 0.39 ± 0.07 with the assumption of dust particles (Fig. 15c). The schematic picture for the formations of cloud along a trough and dust plumes normal to a trough is given in Fig. 8.

The presence of the plume systems, which are oriented in the direction of atmospheric flow and become deeper and more disordered downstream, allows the wind system on the northern polar cap in summer to be constrained to some degree. The plumes are generally aligned normal to the troughs, and in a direction pointing outward from the pole. This agrees roughly with mapping of polar wind patterns on the basis of surficial erosional markings (Howard, 2000). Given the observation of lifted aerosol, it would seem that this polar wind system can become extremely strong. Depending on density of the air, winds in the neighborhood of 30–40 m/s are needed to lift dust (Greeley et al., 1992). As discussed by Howard (2000), the nature of the low-level flow on the martian polar caps indicated by the erosional markings, and now by clouds and observed dust lifting, is consistent with a katabatic wind model: cool air draining off the cold, high center of the polar caps—although the speeds necessary to lift dust could require enhancements to the katabatic winds by the thermal tide and/or by large scale eddies. Katabatic winds off the North Polar cap using a mesoscale model has been studied by Tyler and Barnes (2005). Their model successfully produced off-cap katabatic winds, however the simulated seasons of $L_s = 120°$, 135°, and 150° are later than the THEMIS observations and the wind speed of less than 7.5 m/s in the polar region is not strong enough to lift dust. An interesting aspect of the northern polar plume observations is that they tend to be found in images taken within a few degrees of L_s of northern summer solstice. The northern polar cap does not become fully free of CO_2 ice until roughly $L_s = 100°$, before which time the winds are near their strongest due to the maximal temperature contrast between the CO_2 ice at the center of the cap, and the warm surrounding regolith. Once the CO_2 is fully removed, cap center temperatures jump by as much as 60 K (Titus et al., 2003); this change may be associated with a sharp decrease in katabatic wind strength.

With regards to the dust source, we are left with the problem of the origin of this material. Association with the troughs proffers the possibility of erosion of the material making up

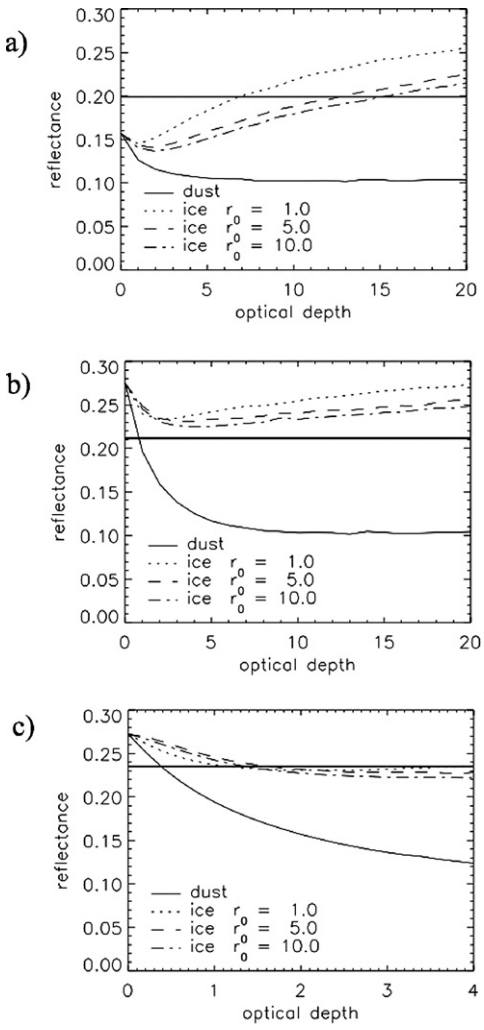

Fig. 15. Same as Fig. 5 but (a) for the cloud appeared over the polar layer seen in Fig. 14a. The thick solid line shows the observed reflectance. The estimated optical depths are at the interactions with the simulated lines. Dust particles are ruled out as the composition; (b) for the storms over the CO_2 ice with the Lambert albedo of 0.72 near the polar layer seen in Fig. 14c. It seems to consist of dust particles; (c) for clouds over the CO_2 ice near the polar layer seen in Fig. 14d. It can consist of dust, ice particles or both.

the layered deposits themselves. It is not clear from the imaging whether the dust (should it be dust) is ancient in this sense, or simply the accumulated fall-out material from the previous winter's dust storm activity.

3.2.3. *Dust devils and tracks*

Dust devils are devilishly difficult to find in THEMIS images for two reasons. First, the pixel size of the images poorly resolves the dust vortices and therefore makes them more difficult to detect than in MOC NA images—though copious dust devils have been seen even in the MOC WA imagery at certain locations (Fisher et al., 2005). Second, and probably more importantly, the later local time of the Odyssey orbit (4–6 p.m.) means is less favored for dust devil development (Renno et al., 1998). The most active site for dust devils on Mars observed by MOC is in Amazonis, where sufficient dust devils in MOC WA images have been detected to allow seasonal evolution studies to be undertaken and correlation with thermal data from TES (Fisher et al., 2005). This same study examined THEMIS VIS images acquired in the first year for this same study region, but found none at the late afternoon local time of THEMIS.

Detecting dust devils in THEMIS images becomes a significantly less profitable game of chance than with MOC imagery—but one that, if won, can have a somewhat higher pay-off. Specifically, Cushing et al. (2005) found a dust devil atop Arsia Mons that simultaneously appears in a THEMIS VIS and IR image. From the combined imagery, definite identification as dust can be made, as well as an assessment of the surface temperature.

Dust devil tracks are substantially easier to find in THEMIS imagery than dust devils themselves. In our assessment of the first year data, well over a hundred images with dust devil tracks have been found among the total 30,625 images. Some example images are shown in Fig. 16. Given the abundance of tracks in both MOC and THEMIS images, a greater literature on track studies exists (Fisher et al., 2005; Greeley et al., 1992). Most tracks have a somewhat random distribution on a given surface, which is what would be expected for randomly spawned vortices developing within the convective boundary layer (Fig. 16a). The development of dust devils within the boundary layer in this way has been simulated in high-resolution numerical models [so-called large eddy simulation (LES) models (Rafkin et al., 2001; Toigo et al., 2003)]. However, some images show a distinctly non-random pattern of track initiation, with topography playing an apparently important role.

Fig. 16b shows tracks or streaks of removed dust on the floor of Gusev crater. Unlike the example typical dust devil track image with randomly distributed tracks, here the tracks generally clearly emanate from small scale topography (typically craters). This association with "seeding" topography is more commonly associated with wind streaks, which are interpreted to result from direct mechanical interaction of the mean wind with the surface, with potential augmentation by interaction with the topography [see, e.g., discussion of streak mechanisms by Fenton and Richardson (2001) and references therein]. However, there is a good reason to believe that the streaks in Fig. 16b are actually dust devil tracks. First, the morphology of the streaks in this image is quite different from typical dark streaks. Fig. 16b should be compared with Fig. 16c, which shows what are typically mapped as erosional (dark) dust streaks. These are similar in morphology to dark streaks observed to develop on freshly deposited dust in a time-lapse sequence by Szwast et al. (2006), providing strong evidence that these kinds of streaks are genuinely related to mean wind processes. The main difference between streaks in Figs. 16b and 16c is the very linear, sharp nature the streaks in the latter, and the highly irregular and meandering nature of the streaks in the former. In a limited number of cases, tracks in Fig. 16b develop without (apparently) associated topography. Fig. 16b streaks would be unambiguously identified as dust devil tracks were it not for the presence of the topographic seeding. We know from Mars Exploration Rover (MER) Spirit observations that dust devils do occur in Gusev crater (Fig. 16d). On this basis, we take these to be dust devil

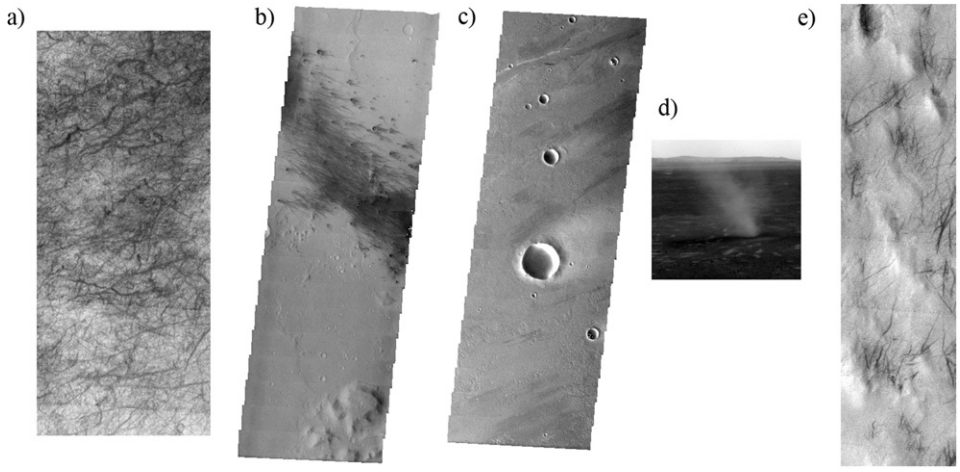

Fig. 16. (a) Example of "typical" dust devil tracks (V00882003), demonstrating no preferential orientation (47.6° S, 141.4° E, $L_s = 333°$). (b) Dust devil tracks in Gusev crater showing topographic control (V00881003), with orientation seemingly in the downwind direction (14.7° S, 175.5° E, $L_s = 333°$). (c) Dark (erosional) wind streaks (V07880021), which are very sharp and linear (17.4° N, 267.3° E, $L_s = 267°$). (d) MER Spirit image of a dust devil captured on Sol 568 (Press Release image from August 19, 2005, marsrovers.jpl.nasa.gov). (e) Dust devil tracks developing preferentially on one side of ridges (V07829003, 47.5° S, 317.3° E, $L_s = 264°$). (a), (b), (c), and (e) are sinusoidal map-projected with north at the top.

tracks. Another example of potentially seeded dust devils is provided in Fig. 16e, which shows tracks preferentially forming on one side of small-scale ridges. The tracks are again highly irregular and meandering, but seem to initiate (or less likely, terminate) at the ridgelines. Several other examples have been found in the THEMIS images.

It is known from modeling that topography can "capture" or "seed" convective upwelling where otherwise the distribution of upwelling would be random—on a larger scale, crater rims can capture convective upwelling, as predicted for the Gusev MER entry site by mesoscale models (Rafkin and Michaels, 2003; Toigo et al., 2003). A slight advantage is provided by the elevated ground through a slope wind effect. Convective plumes can be converted into convective vortices if vertical vorticity is injected into the flow—this maybe happening in Fig. 16e, with the vortices subsequently advected (shed) off the ridge by the mean flow. In the case of the tracks in Fig. 16b, it seems more likely that the topography is functioning as an obstacle that is directly injecting vorticity into the flow. By creating preferential drag on one side of the flow (e.g., on the left side of air passing to the right of the obstacle), rotation can be induced which may be sufficient to cause conversion of irrotational convective plumes into rotational convective vortices. The pairing of tracks on either side of most obstacles suggests this kind of drag process.

While tracks and streaks have been observed extensively within the THEMIS imagery, the coverage is insufficient to make statements about the effectiveness of dust devils and direct wind scouring to modify the albedo of the surface. These issues have been addressed more recently using MOC and TES data by Geissler (2005) and Szwast et al. (2006).

4. Summary and thoughts for the future

This paper summarizes high-resolution atmospheric observations collected during the first mapping year with the Thermal Emission Imaging System (THEMIS) aboard the Mars Odyssey spacecraft. A special atmospheric campaign of targeted observations was implemented that was based on detailed analysis of the lower-resolution Mars Global Surveyor (MGS) Mars Orbiter Camera (MOC) Wide Angle (WA) images (Cantor et al., 2001; Wang and Ingersoll, 2002). Unfortunately, the later local time of the Odyssey orbit meant that features observable in the 2 p.m. MOC WA images were not acquired at high-resolution at the Odyssey local time of 4–6 p.m. Some differences in behavior were not entirely unexpected [e.g., Richardson et al.'s (2002)] discussion of local time dependence of water ice cloud distribution), but the widespread dearth of features in most of the campaign Regions of Interest (ROI) was. This underscores a significant finding of this study (again, not unprecedented, but dramatically illustrated): there is substantial local time variability of most atmospheric phenomena on Mars.

Fortunately, the targeting of THEMIS imaging for surface features did acquire numerous atmospheric features. Due to coverage, these features were mainly observed in the polar regions:

- Cloud fronts in the northern high latitudes appear scalloped suggesting the presence of airmass interfaces. Although the estimated optical depth of the clouds depends on the assumed mode radius of water ice particles, it decreased from the spring to the summer by factor of two or more.
- Clouds forming in thick bands aligned parallel with troughs in the southern polar cap during polar summer. The steady formation of the clouds implies either near saturation of the atmosphere or release of water from the dark troughs. Measured example clouds are extremely bright, with reflectance of 0.4 and height of about 600 m.
- Plumes of dust or particulate ice in flows that transition from impressive, aligned laminar streets to turbulent clouds, and located over the northern polar cap in early northern summer ($L_s = 90°$–$100°$). The plumes suggest

strong winds capable to particulate lifting, and are aligned so as to be consistent with katabatic drainage. The relative short window of activity suggests that the early summer, when the cap center is still covered by CO_2 ice is the period of strongest wind activity. However, the role of waves and/or eddies in augmenting the katabatic winds to the required speed for dust lifting cannot be assessed and may be significant.

- Dust lifting plumes associated with local dust storms were observed in the southern polar region during southern summer. These plumes are morphologically very similar to dust lifting plumes observed on the Earth, and the THEMIS images appear to show higher-resolution samples of the same kinds of features inferred from MOC WA images. The plumes observed appear consistent with a relatively shallow mixed (boundary) layer.
- Using image parallax associated with the way THEMIS collects color images, the heights and zonal advection speeds of clouds have been derived (McConnochie et al., in preparation). These clouds tend to be very high (>45 km), located in the tropics and mid-latitudes. This elevation could be consistent with CO_2 rather than water ice clouds.
- A very limited number of dust devils (Cushing et al., 2005) and many more dust devil tracks have been observed. The much fewer dust devils observed by THEMIS at the Amazonis site of frequent dust devil activity observed by MOC, suggests that at this location, dust devil activity has shut down by the late afternoon (Fisher et al., 2005). While most dust devil tracks observed by THEMIS tend to be either roughly straight or highly disordered (with little intermediate structure seen), some show close association with surface topographic features. This suggests that differential surface drag or "convective seeding" may be important in some cases for dust devil formation.
- Lee wave clouds were abundantly evident in THEMIS images, suggesting a widespread occurrence of stable boundary layer conditions.
- Although specifically targeted, we found very few examples of convective cloud systems (such as the cellular convection clouds seen by MOC—see Fig. 2). This is consistent with the decay of convective activity by the local time of the THEMIS observations.

The local time of the Mars Odyssey orbiter was useful for allowing access to a different mode of martian atmospheric behavior; however, THEMIS was probably not the ideal instrument to first probe this arena because of the need to target the observations. As Mars Odyssey is moved back to earlier local times, the possibility of capturing at high resolution systems observed by MOC WA reappears, and it would therefore be very useful to repeat the original atmospheric campaign once the local time has drifted back to near the early afternoon local time of MGS.

Acknowledgments

We acquired the THEMIS visible data from the THEMIS Public Data Releases, Mars Space Flight Facility, Arizona State University (http://themis-data.asu.edu). THEMIS data are map projected with Integrated Software for Imagers and Spectrometers (ISIS) provided by USGS. TES data are downloaded from the Mars Global Surveyor Archive at the PDS Geoscience Node and analyzed with a software Vanilla provided by Mars Space Flight Facility, Arizona State University. This work was partially supported by a NASA Mars Data Analysis Program grant to Caltech. We thank to Dr. Philip James and an anonymous reviewer for their useful comments.

References

Barnes, J.R., Pollack, J.B., Haberle, R.M., Leovy, C.B., Zurek, R.W., Lee, H., Schaeffer, J., 1993. Mars atmospheric dynamics as simulated by the Nasa Ames General-Circulation model. 2. Transient baroclinic eddies. J. Geophys. Res. 98, 3125–3148.

Bibring, J.P., and 13 colleagues, 2004. Perennial water ice identified in the south polar cap of Mars. Nature 428, 627–630.

Briggs, G.A., Baum, W.A., Barnes, J., 1979. Viking orbiter imaging observations of dust in the martian atmosphere. J. Geophys. Res. 84, 2795–2820.

Burk, S.D., 1976. Diurnal winds near martian polar caps. J. Atmos. Sci. 33, 923–939.

Cantor, B.A., James, P.B., Caplinger, M., Wolff, M.J., 2001. Martian dust storms: 1999 Mars Orbiter Camera observations. J. Geophys. Res. 106, 23653–23687.

Cantor, B., Malin, M., Edgett, K.S., 2002. Multiyear Mars Orbiter Camera (MOC) observations of repeated martian weather phenomena during the northern summer season. J. Geophys. Res. 107, doi:10.1029/2001JE01588.

Cantor, B.A., Kanak, K.M., Edgett, K.S., 2006. Mars Orbiter Camera observations of martian dust devils and their tracks (September 1997 to January 2006) and evaluation of theoretical vortex models. J. Geophys. Res. 111, doi:10.1029/2006JE002700.

Christensen, P.R., and 25 colleagues, 2001. Mars Global Surveyor Thermal Emission Spectrometer experiment: Investigation description and surface science results. J. Geophys. Res. 106, 23823–23871.

Christensen, P.R., and 25 colleagues, 2003. Morphology and composition of the surface of Mars: Mars Odyssey THEMIS results. Science 300, 2056–2061.

Christensen, P.R., and 10 colleagues, 2004. The Thermal Emission Imaging System (THEMIS) for the Mars 2001 Odyssey Mission. Space Sci. Rev. 110, 85–130.

Clancy, R.T., Sandor, B.J., 1998. CO_2 ice clouds in the upper atmosphere of Mars. Geophys. Res. Lett. 25, 489–492.

Clancy, R.T., Wolff, M.J., Whitney, B.A., Cantor, B.A., Smith, M.D., 2007. Mars equatorial mesospheric clouds: Global occurrence and physical properties from Mars Global Surveyor Thermal Emission Spectrometer and Mars Orbiter Camera limb observations. J. Geophys. Res. 112, doi:10.1029/2006JE002805.

Cushing, G.E., Titus, T.N., Christensen, P.R., 2005. THEMIS VIS and IR observations of a high-altitude martian dust devil. Geophys. Res. Lett. 32, doi:10.1029/2005GL024478.

Evans, K.F., 1998. The spherical harmonics discrete ordinate method for three-dimensional atmospheric radiative transfer. J. Atmos. Sci. 55, 429–446.

Fenton, L.K., Richardson, M.I., 2001. Martian surface winds: Insensitivity to orbital changes and implications for aeolian processes. J. Geophys. Res. 106, 32885–32902.

Fisher, J.A., Richardson, M.I., Newman, C.E., Szwast, M.A., Graf, C., Basu, S., Ewald, S.P., Toigo, A.D., Wilson, R.J., 2005. A survey of martian dust devil activity using mars global surveyor mars orbiter camera images. J. Geophys. Res. 110, doi:10.1029/2003JE002165.

French, R.G., Gierasch, P.J., Popp, B.D., Yerdon, R.J., 1981. Global patterns in cloud forms on Mars. Icarus 45, 468–493.

Geissler, P.E., 2005. Three decades of martian surface changes. J. Geophys. Res. 110, doi:10.1029/2004JE002345.

Greeley, R.L.N., Lee, S., Thomas, P., 1992. Martian Aeolian Processes, Sediments, and Features. Univ. of Arizona Press, Tucson.

Hollingsworth, J.L., Haberle, R.M., Barnes, J.R., Brider, A.F.C., Pollack, J.B., Lee, H., Schaeffer, J., 1996. Orographic control of storm zones on Mars. Nature 380, 413–416.

Howard, A.D., 2000. The role of eolian processes in forming surface features of the martian polar layered deposits. Icarus 144, 267–288.

James, P.B., 1982. The clouds of Mars as seen by Viking. Adv. Space Res. 2, 67–74.

James, P.B., 1985. Martian local durt storms. In: Hunt, G.E. (Ed.), Recent advances in planetary meteorology. Cambridge Univ. Press, Cambridge, pp. 85–99.

Jaquin, F., 1989. The Middle Martian Atmosphere. Cornell Univ., Ithaca.

Jaquin, F., Gierasch, P., Kahn, R., 1986. The vertical structure of limb hazes in the martian atmosphere. Icarus 68, 442–461.

Kahn, R., 1984. The spatial and seasonal distribution of martian clouds and some meteorological implications. J. Geophys. Res. 89, 6671–6688.

Kahn, R., 1995. Temperature-measurements of a martian local dust storm. J. Geophys. Res. 100, 5265–5275.

Litvak, M.L., Mitrofanov, I.G., Kozyrev, A.S., Sanin, A.B., Tretyakov, V.I., Boynton, W.V., Kelly, N.J., Hamara, D., Saunders, R.S., 2007. Long-term observations of southern winters on Mars: Estimations of column thickness, mass, and volume density of the seasonal CO_2 deposit from HEND/Odyssey data. J. Geophys. Res. 112, doi:10.1029/2006JE002832.

Malin, M.C., Edgett, K.S., 2001. Mars Global Surveyor Mars Orbiter Camera: Interplanetary cruise through primary mission. J. Geophys. Res. 106, 23429–23570.

Markiewicz, W.J., Sablotny, R.M., Keller, H.U., Thomas, N., Titov, D., Smith, P.H., 1999. Optical properties of the martian aerosols as derived from Imager for Mars Pathfinder midday sky brightness data. J. Geophys. Res. 104, 9009–9017.

McConnochie, T.H., Bell, J.F., Savransky, D., Mehall, G., Caplinger, M., Christensen, P.R., Cherednik, L., Bender, K., Dombovari, A., 2006. Calibration and in-flight performance of the Mars Odyssey Thermal Emission Imaging System visible imaging subsystem (THEMIS VIS). J. Geophys. Res. 111, doi:10.1029/2006JE002568.

Montmessin, F., and 10 colleagues, 2006. Subvisible CO_2 ice clouds detected in the mesosphere of Mars. Icarus 183, 403–410.

Pirraglia, J.A., 1976. Martian atmospheric Lee waves. Icarus 27, 517–530.

Rafkin, S.C.R., Michaels, T.I., 2003. Meteorological predictions for 2003 Mars Exploration Rover high-priority landing sites. J. Geophys. Res. 108, doi:10.1029/2002JE002027.

Rafkin, S.C.R., Haberle, R.M., Michaels, T.I., 2001. The Mars regional atmospheric modeling system: Model description and selected simulations. Icarus 151, 228–256.

Renno, N.O., Burkett, M.L., Larkin, M.P., 1998. A simple thermodynamical theory for dust devils. J. Atmos. Sci. 55, 3244–3252.

Richardson, M.I., Wilson, R.J., Rodin, A.V., 2002. Water ice clouds in the martian atmosphere: General circulation model experiments with a simple cloud scheme. J. Geophys. Res. 107, doi:10.1029/2001JE001804.

Saunders, R.S., and 19 colleagues, 2004. 2001 Mars Odyssey mission summary. Space Sci. Rev. 110, 1–36.

Schofield, J.T., Barnes, J.R., Crisp, D., Haberle, R.M., Larsen, S., Magalhaes, J.A., Murphy, J.R., Seiff, A., Wilson, G., 1997. The Mars Pathfinder atmospheric structure investigation meteorology (ASI/MET) experiment. Science 278, 1752–1758.

Siili, T., Haberle, R.M., Murphy, J.R., 1997. Sensitivity of martian southern polar cap edge winds and surface stresses to dust optical thickness and to the large-scale sublimation flow. Adv. Space Res. 19, 1241–1244.

Smith, M.D., Bandfield, J.L., Christensen, P.R., Richardson, M.I., 2003. Thermal Emission Imaging System (THEMIS) infrared observations of atmospheric dust and water ice cloud optical depth. J. Geophys. Res. 108, doi:10.1029/2003JE002115.

Smith, P.H., and 25 colleagues, 1997. Results from the Mars Pathfinder Camera. Science 278, 1758–1765.

Strausberg, M.J., Wang, H.Q., Richardson, M.I., Ewald, S.P., Toigo, A.D., 2005. Observations of the initiation and evolution of the 2001 Mars global dust storm. J. Geophys. Res. 110, doi:10.1029/2004JE002361.

Szwast, M.A., Richardson, M.I., Vasavada, A.R., 2006. Surface dust redistribution on Mars as observed by the Mars Global Surveyor and Viking orbiters. J. Geophys. Res. 111, doi:10.1029/2005JE002485.

Titus, T.N., Kieffer, H.H., Christensen, P.R., 2003. Exposed water ice discovered near the south pole of Mars. Science 299, 1048–1051.

Toigo, A.D., Richardson, M.I., Ewald, S.P., Gierasch, P.J., 2003. Numerical simulation of martian dust devils. J. Geophys. Res. 108, doi:10.1029/2002JE002002.

Tyler, D., Barnes, J.R., 2005. A mesoscale model study of summertime atmospheric circulations in the north polar region of Mars. J. Geophys. Res. 110, doi:10.1029/2004JE002356.

Wang, H.Q., Ingersoll, A.P., 2002. Martian clouds observed by Mars Global Surveyor Mars Orbiter Camera. J. Geophys. Res. 107, doi:10.1029/2001JE001815.

Wang, H.Q., Ingersoll, A.P., 2003. Cloud-tracked winds for the first Mars Global Surveyor mapping year. J. Geophys. Res. 108, doi:10.1029/2003JE002107.

Wang, H.Q., Zurek, R.W., Richardson, M.I., 2005. Relationship between frontal dust storms and transient eddy activity in the northern hemisphere of Mars as observed by Mars Global Surveyor. J. Geophys. Res. 110, doi:10.1029/2005JE002423.

Warren, S.G., 1984. Optical-constants of ice from the ultraviolet to the microwave. Appl. Opt. 23, 1206–1225.

Young, C.S., Kristovich, D.A.R., Hjelmfelt, M.R., Foster, R.C., 2002. Rolls, streets, waves, and more—A review of quasi-two-dimensional structures in the atmospheric boundary layer. Bull. Am. Meteorol. Soc. 83, 997–1271.

Zurek, R.W., 1992. Comparative Aspects of the Climate of Mars—An Introduction to the Current Atmosphere. Univ. of Arizona Press, Tucson.